SAND2011-9421 C

SAND2011-9421C

Particle Image Velocimetry of a Three-Dimensional Supersonic Cavity Flow

Steven J. Beresh,* Justin L. Wagner,† and Brian O. M. Pruett‡
Sandia National Laboratories, Albuquerque, NM, 87185

Particle image velocimetry measurements have been conducted for supersonic flow over a three-dimensional cavity of variable width using two different experimental configurations. Two-component data were acquired of the entire streamwise extent of the cavity, peering partially into the cavity at an angle, which introduced a perspective bias error in the vertical velocity component. Stereoscopic data at the cavity's aft end were obtained using a more complex camera orientation to see much greater depth of the cavity without introducing perspective error. The data reveal the turbulent shear layer over the cavity and the recirculation region within it. Both the mean structure of the recirculation region and the shear layer turbulence intensity were found to be a function of the length-to-width ratio of the cavity. Large-scale turbulent eddies are prominent within the shear layer but not evident in the recirculation region.

Introduction

Flow over a cavity has been studied for many years in a wide range of speed regimes. The most common motivation in high-speed flows concerns aircraft weapons bays, but other flight applications include landing gear wells, open sensor or telescope bays, and flame holders for scramjets. Flow instrumentation based on imaging, ranging from historical schlieren experiments to modern laser-based diagnostics, requires a view into the cavity. In the majority of cases, the most valuable view of the cavity flow is the normal streamwise plane to capture the shear layer shed at the cavity's leading edge.

A practical simplification for many experiments has been to simply test a two-dimensional cavity, in which the cavity encompasses the full extent of the test section and windows may be placed on either side of it for a view laterally through the cavity. This has been the most common solution to providing optical access into the cavity. It has been used for schlieren and shadowgraphy [1-7], laser Doppler velocimetry [4, 8], laser Rayleigh scattering [9, 10], planar laser-induced fluorescence [11, 12], and particle image velocimetry (PIV) similar to the present work [7, 13-21]. Though a simple solution to imaging occlusion, clearly it cannot be used when three-dimensional flow effects must be studied inside more complex cavity geometries. Realistic weapons bays are considerably narrower in the spanwise dimension than in the streamwise dimension, which may introduce an additional flow-field dependence. A few studies have demonstrated that three-dimensional turbulent structures and transverse acoustic modes can be found within a cavity [10, 22-26], suggesting that the length-to-width ratio may be an important parameter describing the nature of the flow within such narrower cavities. A rare published case in which a realistic weapons bay geometry was considered demonstrated that acoustic characteristics can change dramatically as the geometry is altered [27]. These observations motivate the need to image within a three-dimensional cavity, including those with greater geometric complexity than a simple rectangular cutout.

The two-dimensional approach can be extended to three-dimensional rectangular cutouts by growing the thickness of the side windows into the span of the test section and continuing to image the flow normally from the side, but this can create imaging discontinuities and artifacts at the cavity lip between flow inside the cavity and

*Principal Member of the Technical Staff, Engineering Sciences Center, Associate Fellow AIAA, correspondence to: P.O. Box 5800, Mailstop 0825, (505) 844-4618, email: sjberes@sandia.gov
†Senior Member of the Technical Staff, Member AIAA
‡Senior Technologist

This work is supported by Sandia National Laboratories and the United States Department of Energy. Sandia National Laboratories is a multi-program laboratory managed and operated by Sandia Corporation, a wholly owned subsidiary of Lockheed Martin Corporation, for the U.S. Department of Energy's National Nuclear Security Administration under contract DE-AC04-94AL85000.

flow outside it [28, 29]. Another approach has been to extrude a three-dimensional cavity beyond the lower test section wall such that a window in the side of the cavity is accessible from below the test section, but this can view only the interior of the cavity and not the flow above it [30]. Other experiments have simply imaged above the lip of the cavity and foregone any measurements within it [31-33].

Surprisingly, there appears to be no example of an experiment in which a camera peered into the cavity at an angle, after which the resulting images could be unwarped. This approach forms the subject of the present document. Admittedly, a three-dimensional cavity even as simple as a rectangular cutout requires awkward camera angles to peer into the cavity, which may pose limitations to the resulting data or induce measurement errors. Nonetheless, several advantages are provided by canted viewing angles, beyond the obvious ability to view the interior of three-dimensional cavities. No discontinuity will arise at the cavity lip as a result of viewing through different window thicknesses. The configuration is straightforward to adapt to the greater complexities of wind tunnel models of realistic flight hardware. The imaging plane can be kept in focus despite the viewing angle using scheimpflug focusing, which has become commonplace in stereoscopic PIV. Correction for the perspective distortion is inherent in standard camera calibration algorithms also widely used in stereoscopic PIV.

The goal of the current work is to develop PIV techniques to acquire data in the streamwise normal plane within three-dimensional cavities. Presently, that simply refers to rectangular cutouts that do not span the width of the test section, but the measurement techniques implemented herein are intended for future use in considerably more complex geometries replicating features found in real aircraft weapon bays. Two different PIV experiments have been conducted. A two-component configuration was used to survey the entire streamwise extent of the shear layer in the cavity, whereas a stereoscopic configuration provided more complete data in a smaller field of view near the trailing edge of the cavity. Moreover, the two-component velocity data suffer from a perspective error due to the angled cameras that cannot be corrected, which does not occur in the stereoscopic data. The implementation of the two PIV configurations is discussed in the present document, as are the differences in the resulting data from the two approaches.

Experimental Apparatus

Trisonic Wind Tunnel

Experiments were performed in Sandia's Trisonic Wind Tunnel (TWT), which is a blowdown-to-atmosphere facility using air as the test gas through a 305 × 305 mm^2 (12 × 12 $inch^2$) rectangular test section enclosed within a pressurized plenum. In its supersonic configuration, the TWT's Mach numbers are varied by exchanging the top and bottom walls of the planar nozzle; Machs 1.5, 2.0, 2.5, and 3.0 are available. The tunnel originally was designed for sting-mounted measurements near the centerline of the test section, whereas the contoured nozzle walls continue nearly to the end of the test section. Though the testing location is still within the nozzle curvature, the supersonic expansion is complete in the vicinity of the centerline where experiments are conducted; i.e., the measurements lie within the "test rhombus" of the test section as evidenced by wind tunnel calibrations.

The absence of a flat working surface in the supersonic test sections poses a problem both for optical access for laser diagnostics and wall-mounted experimental configurations. The tunnel side walls have been used for some experiments, but are insufficient for imaging diagnostics. As a solution, a half-nozzle test section has been designed in which the top wall of each supersonic nozzle is retained and a single bottom wall replaces the lower supersonic nozzle wall. The new lower wall extends the inlet contour of the tunnel and then fairs into a flat surface at what previously would have been the test section centerline. This provides a flat plate working surface within the test rhombus of the supersonic expansion with convenient optical access. Further, it is compatible with each of the supersonic upper nozzles, excepting the Mach 3 contour, at which the additional boundary layer growth on the new half-nozzle wall prevents passage of the starting shock. The resulting half-nozzle test section therefore is 152 mm (6 inch) high and 305 mm (12 inch) wide. The half-nozzle configuration has been calibrated at each Mach number using wall pressure taps and Pitot surveys of the boundary layer, showing flow conditions to be sufficiently uniform and the wall boundary layer developing under equilibrium conditions at the testing location. A photograph of the half-nozzle test section is given in Fig. 1, with the near side wall removed to reveal the wall curvature of the upper supersonic contour and the lower half-nozzle flat plate.

Current experiments were conducted at Machs 1.5, 2.0, and 2.5, but only data acquired at Mach 1.5 are given in the present document as these are sufficient to discuss the measurement implementation. The Mach 1.5 data used a stagnation pressure of 261 kPa (38 psia) to achieve a unit Reynolds number of 36×10^{-6} m^{-1} (11×10^{-6} ft^{-1}). The wind tunnel stagnation temperature T_0 is fixed at 321K ± 2K by heating in the storage tanks, and the wall temperature is effectively constant at ambient conditions, T_w=307K ± 3K, though T_w tends to drift upward within

this range as the wall warms during the course of a day. Earlier Pitot probe surveys measured the 99%-velocity incoming boundary layer thickness as 12.4 mm (0.49 inch).

Cavity Hardware

The three-dimensional cavity of the present experiments is simply a rectangular hole in the half-nozzle flat plate. It is designed into an insert plate in the floor of the test section, as shown in Fig. 2. The floor of the cavity is a BK7 glass flat optically coated for anti-reflection at 532 nm, so that the laser sheet for the particle image velocimetry measurements can be directed into the cavity from below. The cavity has dimensions 127 × 127 mm^2 (5 × 5 $inch^2$) with a nominal depth of 25.4 mm (1 inch) that was measured to be 25.9 mm (1.02 inch) in practice. The discrepancy in cavity depth is due to the actual versus predicted crush of a gasket between the glass flat and the lower edge of the cavity walls. In addition to the widest cavity dimensions of 127 × 127 mm^2, insert blocks can be bolted against the cavity side walls to reduce the cavity width for additional tests. This is used to create cavities of 127 × 76 mm^2 (5 × 3 $inch^2$) and 127 × 25 mm^2 (5 × 1 $inch^2$); the cavity depth is not changed.

Particle Image Velocimetry System

The TWT is seeded by a thermal smoke generator (Corona Vi-Count 5000) that produces a large quantity of particles typically 0.2 - 0.3 µm in diameter from a mineral oil base. Particles are delivered to the TWT's stagnation chamber upstream of the flow conditioning section through a series of pipes and tubes, in which agglomeration of the particles occurs. Previous measurement of the *in-situ* particle response across a shock wave generated by a wedge shows the particle size to be 0.7 - 0.8 µm. Stokes numbers have been estimated as 0.04 based on *a posteriori* measurements of typical cavity shear layer eddies, which is sufficiently small to rapidly attain the local velocity even in the presence of velocity gradients in the shear layer [34, 35]. Inspection of PIV images of the recirculation region in the cavity shows that although the particle density drops, sufficient particles are retained for high vector quality in all regions.

The light source for the PIV system was a frequency-doubled dual-cavity Nd:YAG laser (Spectra Physics PIV-400) that produced about 400 mJ per beam. The beams were formed into coplanar sheets and directed into the test section from beneath the wind tunnel, then entered the cavity through the window forming its floor. The laser sheet thickness was 1.0 mm in all cases, and the time between pulses was 1.488 µs for the Mach 1.5 data in the two-component configuration and 1.007 µs in the stereoscopic configuration. The laser sheet was aligned to the spanwise center of the cavity and filled the entire streamwise length of the cavity.

Scattered laser light was collected by interline-transfer CCD cameras (LaVision Imager ProX 4MP) with a resolution of 2048 × 2048 pixels digitized at 14 bits. The two cameras were equipped with 105 mm lenses for the two-component PIV and 200 mm lenses for the stereoscopic PIV; in both cases, the lenses were mounted on Scheimpflug platforms to create an oblique focal plane aligned with the laser sheet. For the two-component configuration, the cameras were placed side by side to survey an extent of the cavity twice as large in the streamwise

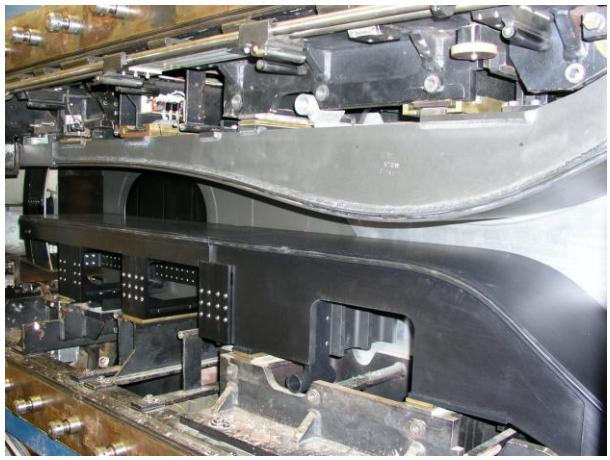

Fig. 1: Photograph of the half-nozzle supersonic test section of Sandia's Trisonic Wind Tunnel, with the near side wall removed to reveal the wall curvature. Flow is from right to left.

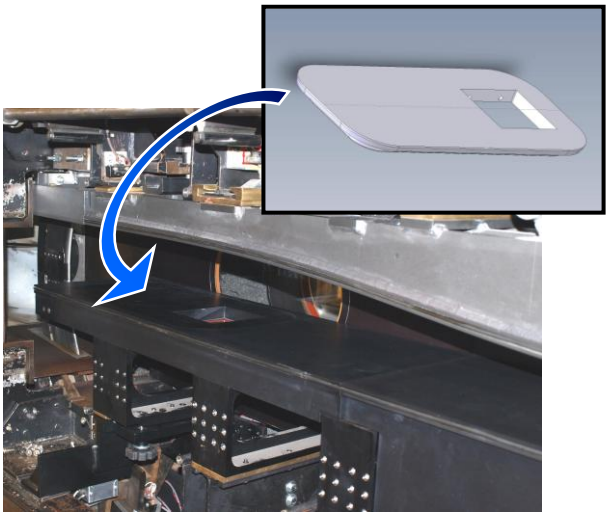

Fig. 2: The 127 × 127 mm^2 (5 × 5 $inch^2$) cavity installed into the floor of the half-nozzle test section.

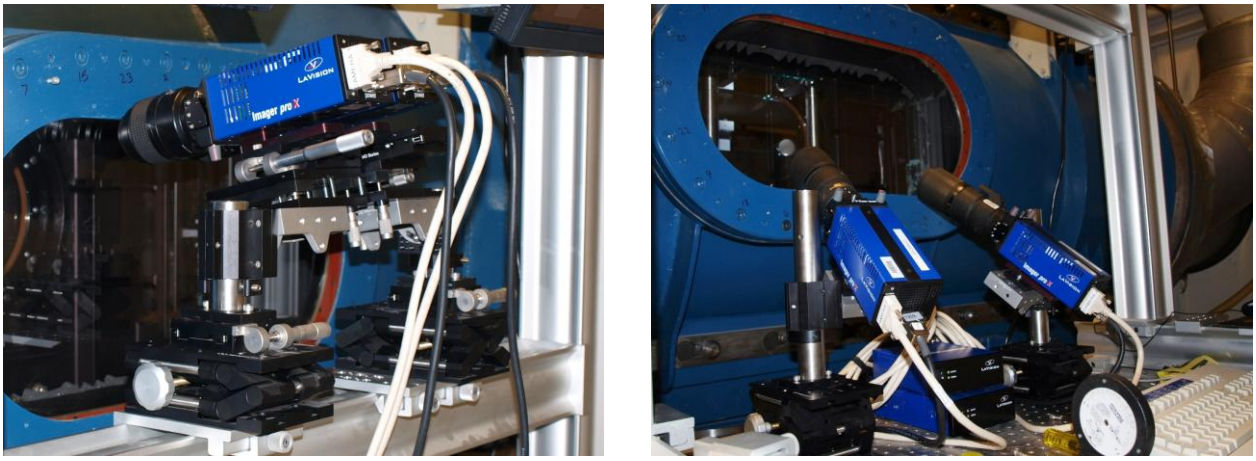

(a) **(b)**

Fig. 3: Photographs of the camera angles to peer into the cavity; (a) two-component PIV; (b) stereoscopic PIV. In the stereoscopic case, an additional turning mirror is mounted inside the plenum near the top of the window.

dimension as in the vertical dimension. The cameras peered down into the cavity as shown in Fig. 3a at an angle of 11 deg, and Scheimpflug focusing was used to keep the images in focus despite the camera angle. An alignment target placed at the laser sheet location was used to produce a calibration that could account for the variable magnification due to the viewing angle.

For stereoscopic data, the cameras viewed the imaging region using compound angles, where half-angles of 12 deg separated the two cameras in the streamwise plane and both were angled identically in the vertical plane at 38 deg to look into the cavity. The 12 deg streamwise half-angle is sub-optimal for stereoscopic measurements, but a greater angle would have suffered occlusion of the field of view by the trailing edge of the cavity. Two-axis scheimpflug focusing is required for this configuration, which first was discussed by Walker [36] and subsequently has become standard in tomographic PIV [37]. A smaller lens aperture (large f-number) aided focusing by increasing the depth of field. To increase the vertical angle possible given optical access restrictions of the TWT, a mirror was rigidly mounted inside the plenum near the top wall to reflect scattered light back towards the cameras at a sharper angle; wind tunnel vibrations were found not to pose a difficulty. The stereoscopic camera arrangement is shown in Fig. 3b. Stereoscopic camera calibrations were accomplished by placing a single-plane alignment target in the position of the laser sheet, then scanning it through the volume of the laser sheet to acquire seven planes of calibration data, which were calibrated using a polynomial fit.

Data were processed using LaVision's DaVis v7.2, where image pairs were interrogated with an initial pass using 64 × 64 pixel interrogation windows, followed by two iterations of 32 × 32 pixel interrogation windows, incorporating adaptive window offsets and image deformation based upon local velocity gradients. A 50% overlap in the interrogation windows was used as well to oversample the velocity fields. The resulting vector fields were validated based upon signal-to-noise ratio, nearest-neighbor comparisons, and allowable velocity range.

Results and Discussion

Two-Component Measurements

At Mach 1.5, about 800 image pairs were acquired from each camera for the 127 × 127 mm^2 (5 × 5 inch^2) cavity, henceforth simply termed the 5 × 5 cavity. An additional 500 image pairs were acquired for the 5 × 3 cavity and 300 image pairs for the 5 × 1 cavity. Velocity fields acquired by the two side-by-side cameras were combined into a single vector field, which is plotted in Fig. 4 for each of the three cavity widths. The mean streamwise velocity field is shown with mean vectors overlaid. Vectors are subsampled by a factor of eight in the streamwise direction and a factor of two in the vertical direction. The coordinate system is chosen such that the u component lies in the streamwise direction and the v component is in the vertical direction, positive away from the cavity; the w component is chosen for a right-handed coordinate system. The origin of the coordinate axes is the spanwise center of the cavity leading edge. Dimensions are normalized to the cavity depth D.

The measurements shown in Fig. 4a in the 5 × 5 cavity demonstrate that this camera angle can see about 60% of

the depth of the cavity, which is sufficient to capture the entire shear layer and the upper portion of the recirculation region. Reverse velocities can be seen within the recirculation region. The 5 × 3 and 5 × 1 cavities can be viewed 35% and 10% into their depths, respectively, which shows the limitations of the camera view. Some imaging artifacts can be seen in the vector fields. An artificial reduction in the streamwise velocity is visible in the upper left of the vector plots, worst in Fig. 4a, which has been found to be due to background illumination of the forward cavity lip where it extends behind the laser sheet. A more subtle reduction in the streamwise velocity is visible in Figs. 4a and 4b just before the shear layer impinges the aft wall of the cavity; to at least some extent this must be due to the onset of the recirculation region, but it is not clear if this also is artificial due to the laser striking the wall. No reverse velocities are visible in the reduced visibility of the narrower cavities in Figs. 4b and 4c. In Fig. 4c, data clearly do not extend sufficiently deep into the cavity to capture the recirculation region. However, comparing Figs. 4b and 4a, it appears that data for the 5 × 3 cavity of Fig. 4b should be able to display reverse velocities were they present at this height, suggesting that flow in this cavity may differ from the 5 × 5 cavity. This will be discussed at further length using the stereoscopic data.

The streamwise turbulence intensity fields are given in Fig. 5 for the same three conditions, with the mean velocity vectors from Fig. 4 overlaid for reference. The same artifact in the upper left corner seen in Fig. 4 is visible here as well. In addition, Fig. 5b and to a lesser extent Fig. 5c show a horizontal line of elevated intensities at about y/D of 0.3 or 0.4 This is due to light reflections off the lip of the opposite side wall of the cavity, which could not be fully treated by image preprocessing before interrogating the image pairs. Nevertheless, the structure of the turbulence intensity of the shear layer is clear and appears to cover a greater vertical extent than that evident in the mean velocity fields. Elevated turbulence intensity is visible in the recirculation region of the 5 × 5 cavity in Fig. 5a as well. Interestingly, the turbulence intensity magnitudes appear to be somewhat reduced for the 5 × 3 cavity in Fig. 5a as compared to both the 5 × 5 and the 5 × 1 cavities in Fig. 5b.

The mean and turbulent structure of the cavities bear a strong resemblance to previous studies. Despite being a two-dimensional cavity (i.e., full span across the wind tunnel test section) and at a lower Mach number of 0.2, the data of Ukeiley and Murray [15] for a nearly identical length-to-depth ratio are highly similar to Fig. 4a in the width of the shear layer and the shape of the recirculation region. The mean velocity field of Zhuang et al [29] at Mach 2 in a three-dimensional cavity of similar ratio also closely corresponds to Fig. 4a. Ukeiley and Murray [15] and Basley et al [20] find peak streamwise turbulent intensities consistent with the value of about 0.22 shown in Fig. 5a, with Haigermoser et al [18] only a little lower.

Sample instantaneous snapshots of the velocity field are shown in Fig. 6 to display the variety of turbulent eddies that can be found in the cavity, all taken from the 5 × 5 cavity dataset. These vector fields have been spatially low-pass filtered to highlight the large-scale eddies. In these plots, the vectors have been subsampled by four in the streamwise direction and two in the vertical direction, with the vector scale having been altered from Fig. 4. These changes better visualize the instantaneous eddy structure. These vector fields represent the larger dataset by displaying the variety of shear layer undulations and large-scale eddies that can be found in the cavity. Fig. 6b shows very little reverse flow within the cavity, but Figs. 6a and 6c have prominent recirculation. The shear layer of Fig. 6c is quite active, whereas in contrast, Fig. 6a shows a relatively quiescent shear layer. It is the variety of these eddies and how they recirculate within the cavity that give rise to the acoustic properties.

Although the velocity fields shown in Figs. 4-6 reveal considerable useful information about the cavity flow and are consistent with previous studies, they are known to suffer from a velocity bias resulting from the angled view into the cavity. The variable magnification of the image distortion due to off-axis imaging has been corrected to place the velocity vectors accurately in space, but a perspective error remains due to an apparent in-plane displacement created by sensitivity to out-of-plane motion [38, 39]. In the present case, this occurs because the (mostly) vertical velocity component measured normal to the camera axis is no longer aligned with the plane of the laser sheet. The resulting perspective error increases with both camera angle and larger out-of-plane motion, and it is unrecoverable without measurement of the third velocity component. The error may determined as $\varepsilon_v = (\Delta z/\Delta y) \tan\varphi_y$. If the out-of-plane velocity component in the shear layer is comparable to the vertical component, which is a reasonable assumption for a shear layer, this indicates $\varepsilon_v \approx \tan\varphi_y$. The resulting error is nearly 20% in the vertical velocity component for the present camera angle. Nevertheless, the existence of this error does not grossly alter the visualizations of the cavity flow presented in Figs. 4-6, but it does provide an additional motivation for the use of stereoscopic PIV.

Stereoscopic Measurements

To obtain the third velocity component and remove the perspective error in the vertical component, stereoscopic measurements were conducted in the downstream portion of the cavity. The entire cavity cannot be visualized in this case with only the two available cameras without sacrificing spatial resolution (i.e., a rather large field of view),

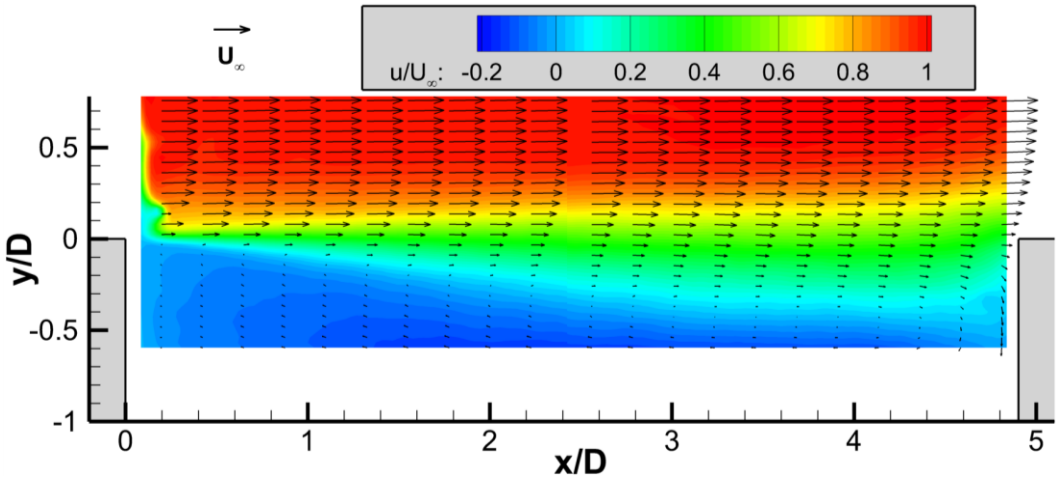

(a)

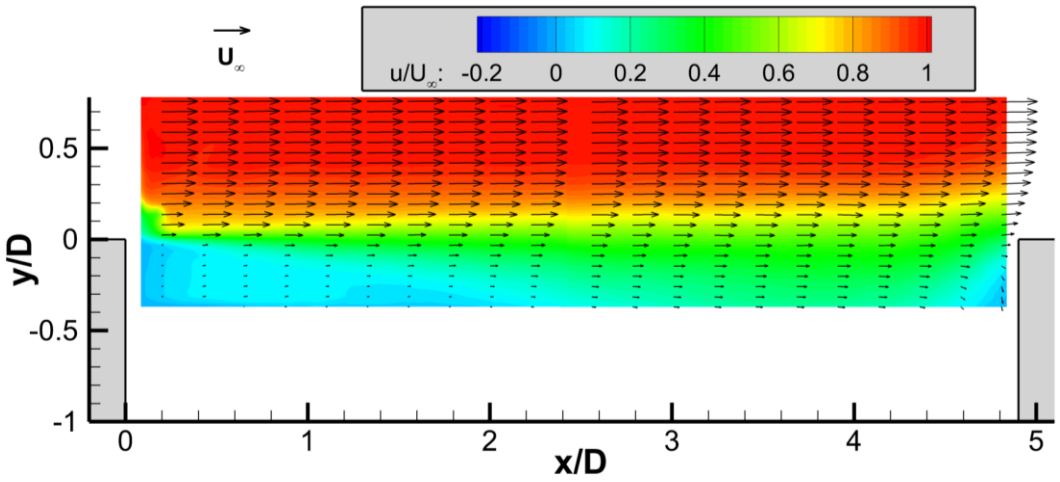

(b)

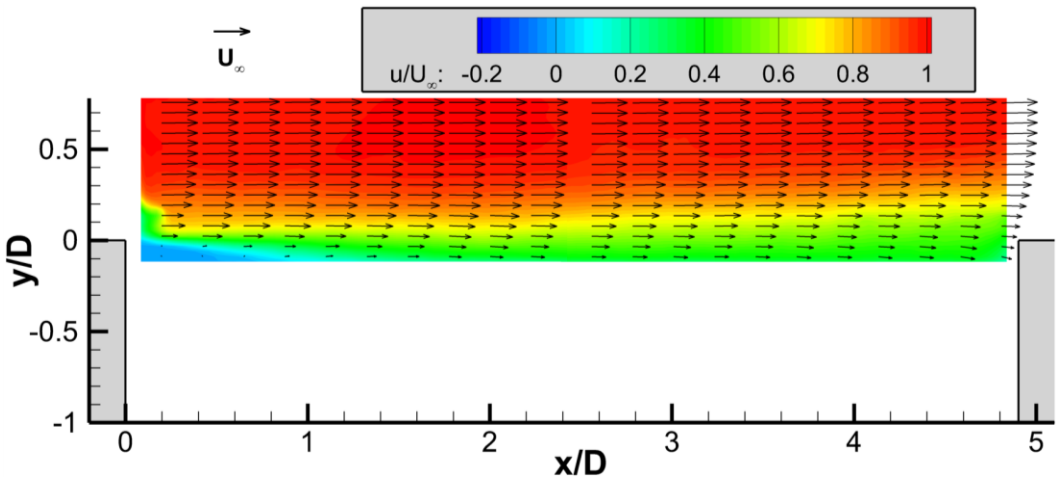

(c)

Fig. 4: Mean velocity fields from two-component PIV for (a) the 127 × 127 mm^2 (5 × 5 inch^2) cavity; (b) 127 × 76 mm^2 (5 × 3 inch^2); (c) 127 × 25 mm^2 (5 × 1 inch^2). Vectors are subsampled by a factor of eight in the streamwise direction and two in the vertical direction.

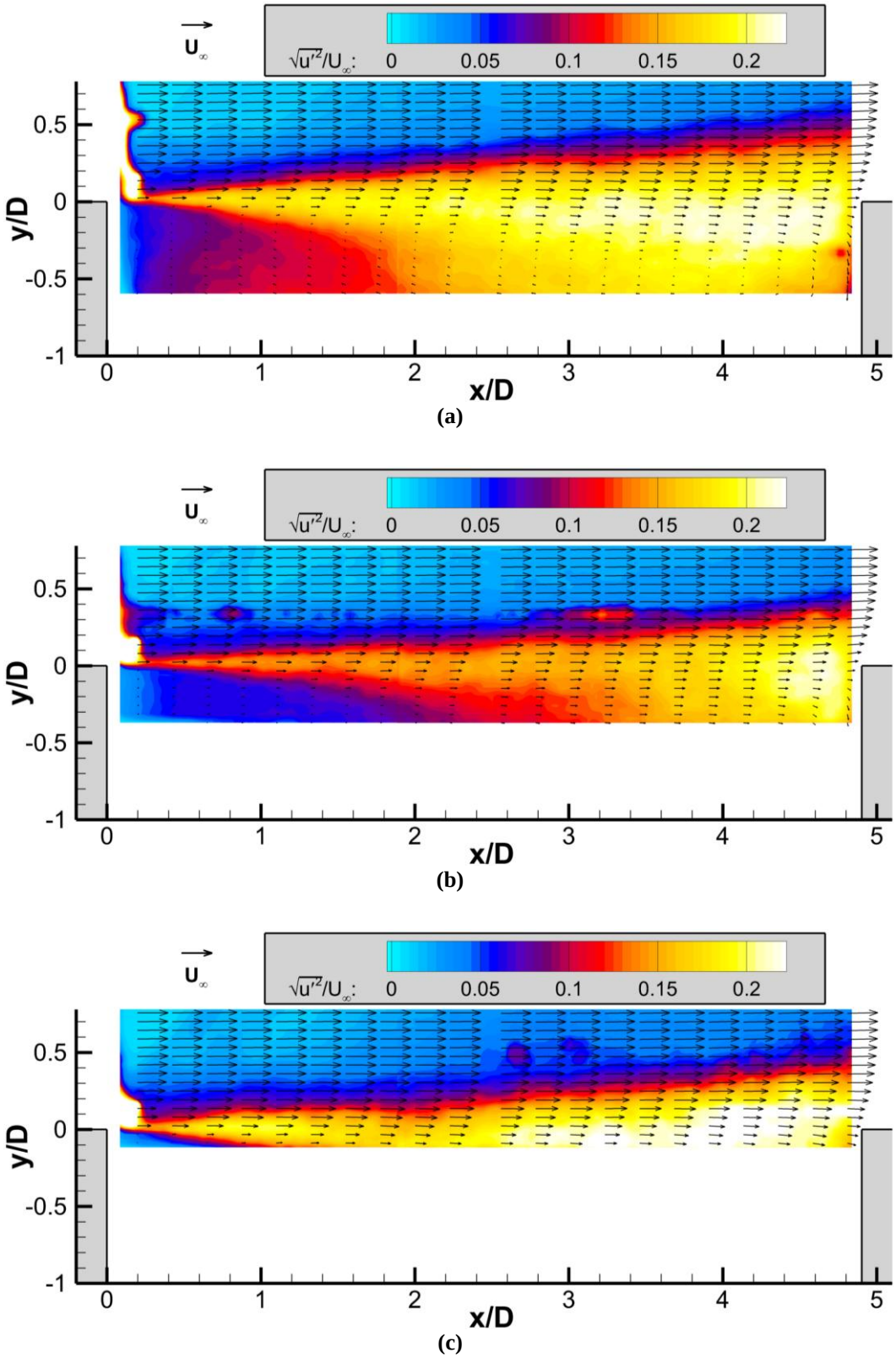

Fig. 5: Streamwise turbulence intensity fields from two-component PIV for (a) the 127 × 127 mm^2 (5 × 5 inch^2) cavity; (b) 127 × 76 mm^2 (5 × 3 inch^2); (c) 127 × 25 mm^2 (5 × 1 inch^2). Vectors are the mean velocity fields of Fig. 4, superposed for reference.

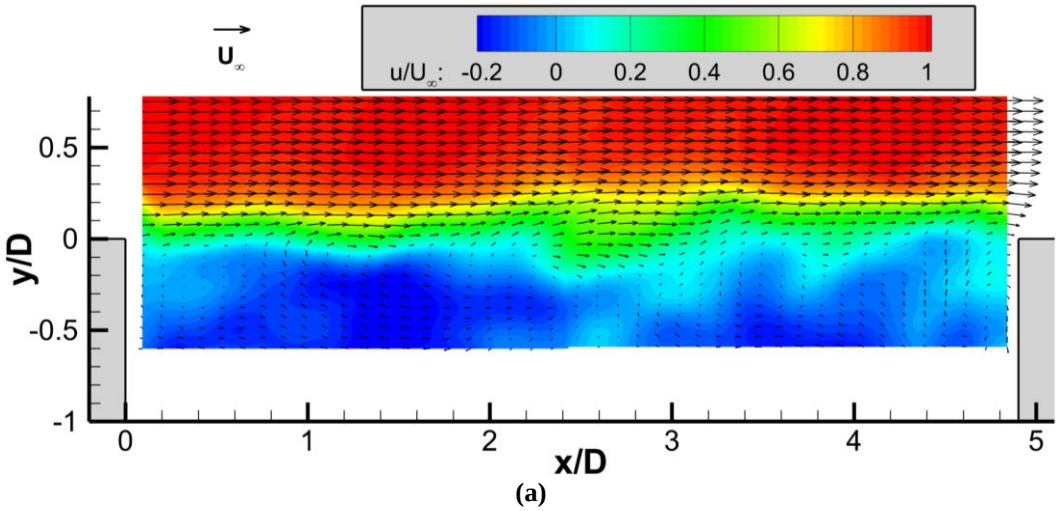

(a)

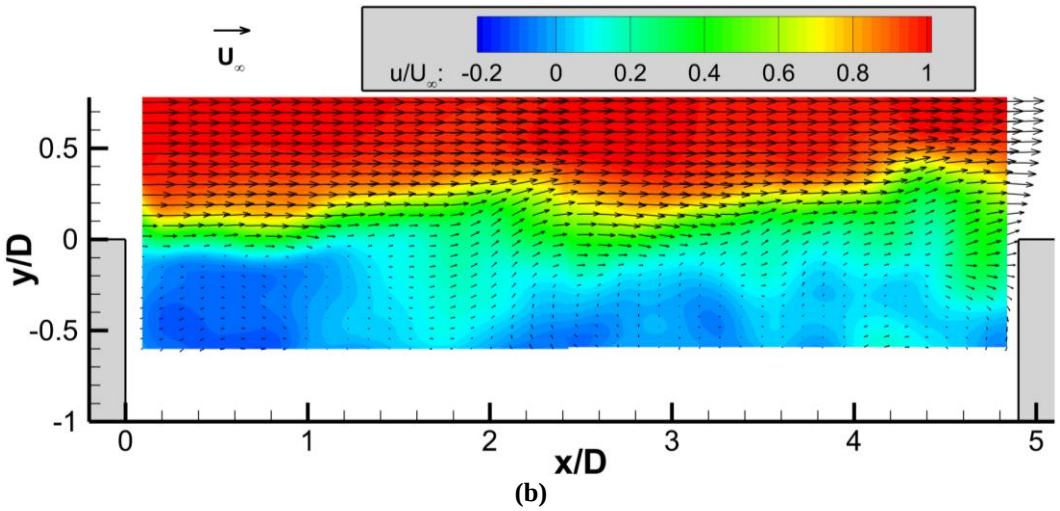

(b)

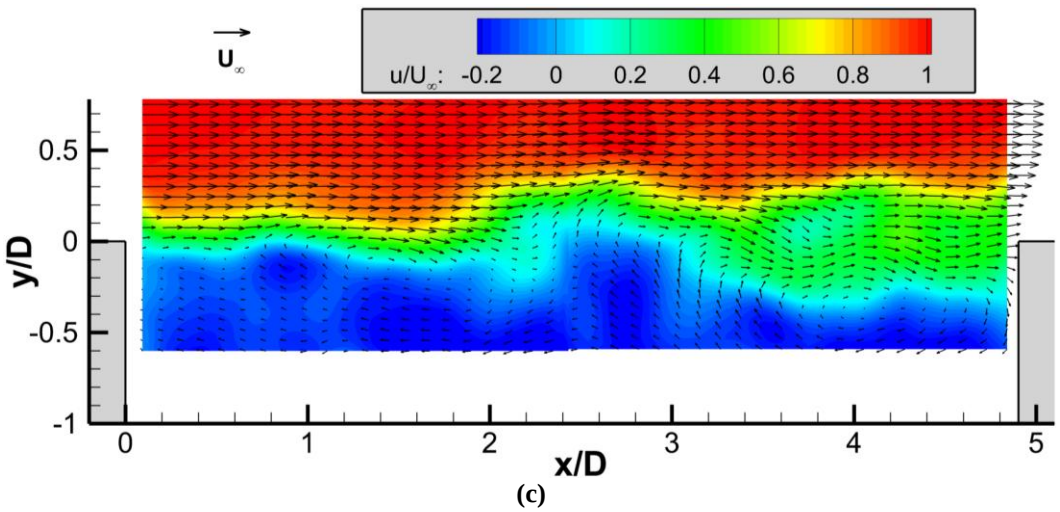

(c)

Fig. 6: Sample instantaneous velocity fields from two-component PIV for the 127 × 127 mm^2 (5 × 5 inch^2) cavity. Vectors are subsampled by a factor of four in the streamwise direction and two in the vertical direction.

so the measurement region focused upon the most turbulent portion of the cavity just before the shear layer impinges upon the aft cavity wall. In addition, as shown in Fig. 3b and discussed earlier, an extra turning mirror placed in the plenum allowed a steeper vertical camera angle to peer deeper into the cavity. Although a similar sharpened camera angle could have been employed for the earlier two-component measurements, this would have substantially increased the perspective error in the vertical component; this is not a consideration for stereoscopic data since all three components are returned.

The resulting mean velocity fields are shown in Fig. 7 for the three cavity widths, based on about 500 realizations per case. It is immediately evident that for the 5 × 5 and the 5 × 3 cavities, measurements reach all the way to the floor of the cavity. In the case of the 5 × 1 cavity, too much occlusion remains from peering over the cavity side wall and only about 30% of the cavity depth is captured; still, this is a considerable improvement over the 10% achieved by the two-component configuration and a fair portion of the shear layer is observed. The mean out-of-plane component is not shown, but was found to be essentially equal to zero throughout the field of view.

The deeper view of the cavity enables a better perspective on the nature of the recirculation region. The largest reverse velocities are seen to reach $0.35U_\infty$ for the 5 × 5 cavity, but only $0.28U_\infty$ for the 5 × 3 cavity. Moreover, the recirculation region lies closer to the cavity floor for the 5 × 3 cavity as compared to the 5 × 5 cavity, with its center located at y/D=-0.75 versus y/D=-0.40, respectively. This is consistent with the two-component observation in Fig. 4 that reverse velocities did not appear at the same region of the cavity. It is not possible to measure sufficiently deep into the cavity for the 5 × 1 case to provide a comparable observation, but those vectors that are visible suggest a higher recirculation region akin to the 5 × 5 cavity.

Turbulent kinetic energy fields for the stereoscopic data are given in Fig. 8, with the mean in-plane velocity vectors of Fig. 7 superposed. The data are a little noisy given the relatively low quantity of individual realizations (500 each) for determining higher-order statistics. Nonetheless, the turbulence structure is clear and differences between the three cavities can be observed, at least on the centerline plane shown by the present measurements. The horizontal line visible in the 5 × 1 cavity at y/D=0.3 is due to background reflections along the lip of the far side wall. In all cases, turbulence within the cavity and below the shear layer itself is nearly as high as within the shear layer. In comparing the 5 × 3 cavity to the 5 × 5 cavity, it is evident that turbulence levels are substantially reduced for the 5 × 3 case. Turbulence in the shear layer of the 5 × 1 cavity is the highest of the three, but closer in nature to the 5 × 5 cavity than the 5 × 3 cavity.

From both the two-component and the stereoscopic data, there does appear to be a difference in the flow within the 5 × 3 cavity as compared to the 5 × 5 and 5 × 1 cavities. For the 5 × 3 cavity, the recirculation region appears smaller and nearer to the wall with weaker reverse flow, and the turbulence levels in both the shear layer and the recirculation region are suppressed. The same trends also were found for the Mach 2 and Mach 2.5 data, indicating that this trend is robust and not an unexplained measurement artifact. Although earlier experiments have detected a three-dimensional nature to recirculation within a cavity of fixed proportions [10, 23] and others measured the variation of acoustic properties as the cavity width was varied [22, 24], a difference in the recirculation structure of the cavity as a function of the cavity length-to-width ratio is not believed to have been reported previously. The structural difference in the recirculation region may be a consequence of spanwise acoustic tones in the cavity that are reinforced at particular widths.

Data Comparison

Figure 9 shows the data from the stereoscopic measurements overlaid on two-component results, with Fig. 9a displaying the mean streamwise velocity field and Figs. 9b and 9c the streamwise and vertical turbulent stresses, respectively. For brevity, only the 5 × 5 cavity is shown. For the streamwise component in Figs. 9a and 9b, the agreement between the two measurement configurations is remarkably good. The stereoscopic data blend seamlessly into the two-component measurements. Data comparisons for the 5 × 3 and 5 × 1 cavities reveal agreement just as good as in Figs. 9a and 9b. However, the vertical turbulent stress in Fig. 9c clearly demonstrates the discrepancy between the two measurements, which can be attributed to the perspective error present in the two-component measurements. The apparent magnitudes of the vertical velocity fluctuations are reduced by the camera angle.

For a more quantitative display of the data comparison, profiles of the mean velocities and turbulent stresses were extracted from the plots of Fig. 9 at two streamwise locations, one near the upstream end of the stereoscopic field of view (x/D=2.4) and one near the downstream end (x/D=4.4). These are shown in Fig. 10 for the mean velocities and Fig. 11 for the turbulent stresses. The mean streamwise velocities in Fig. 10 everywhere agree to within $0.02U_\infty$ and typically are considerably closer than that. Conversely, the curves for the mean vertical component share the same general profile shape, but diverge both in their magnitudes and are offset. The perspective error in the two-component data does not simply diminish the magnitude of the vertical component, but

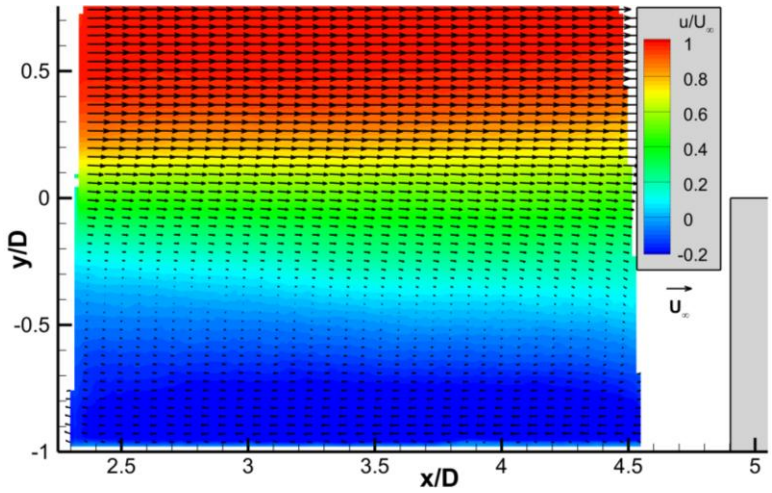

(a)

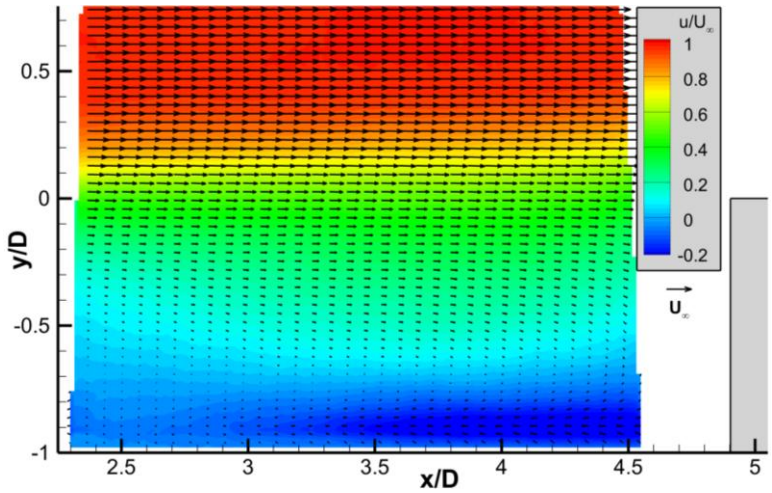

(b)

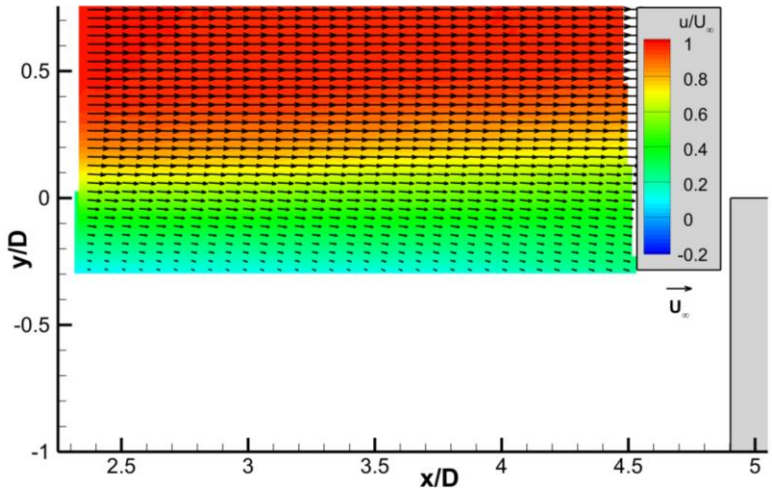

(c)

Fig. 7: Mean velocity fields from stereoscopic PIV for (a) the 127 × 127 mm^2 (5 × 5 inch^2) cavity; (b) 127 × 76 mm^2 (5 × 3 inch^2); (c) 127 × 25 mm^2 (5 × 1 inch^2). Vectors are subsampled by a factor of four in the streamwise direction and two in the vertical direction.

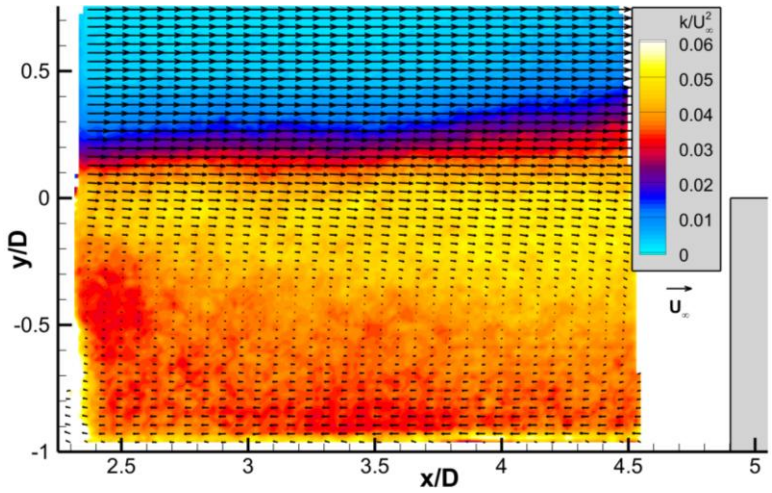

(a)

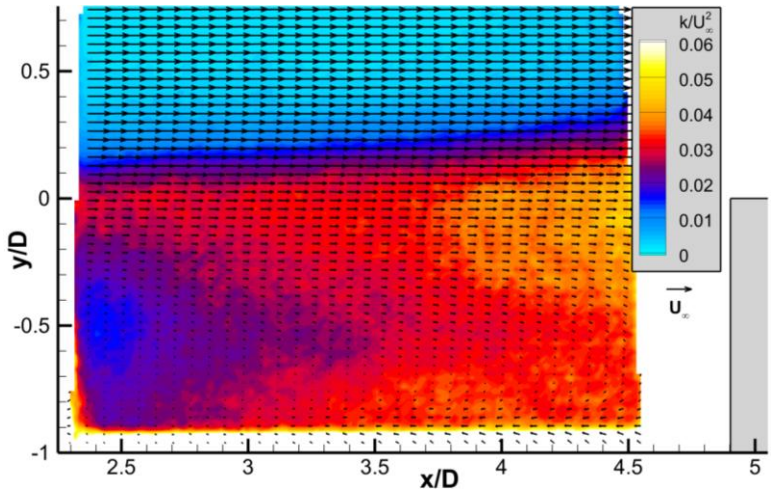

(b)

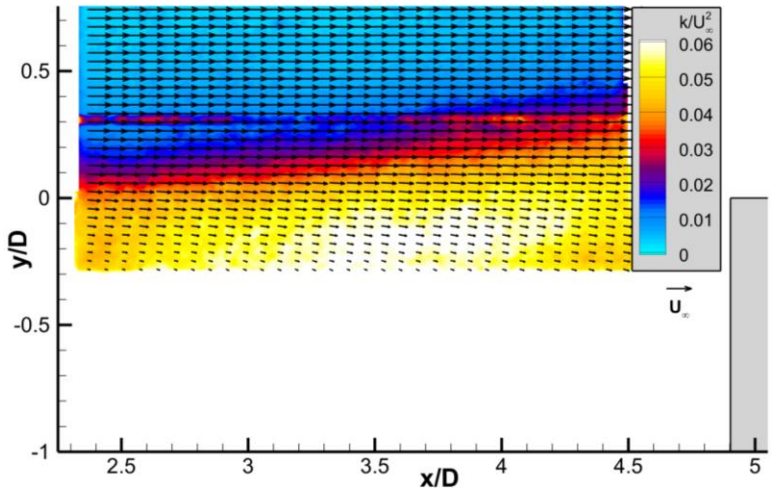

(c)

Fig. 8: Streamwise turbulent kinetic energy fields from stereoscopic PIV for (a) the 127 × 127 mm^2 (5 × 5 inch^2) cavity; (b) 127 × 76 mm^2 (5 × 3 inch^2); (c) 127 × 25 mm^2 (5 × 1 inch^2). Vectors are the mean velocity fields of Fig. 7, superposed for reference.

also introduces a constant bias error. The measurement error in the magnitude appears roughly consistent with the predicted 20%, but it is not clear what is the source of the velocity offset. The greater degree of noise present in the vertical component compared to the streamwise component is simply due to the considerably smaller range of velocities present in the vertical direction, which makes the precision error of the measurement greater relative to the axis scale.

Similar observations may be made about the turbulent stresses shown in Fig. 11. For the streamwise component, agreement between the two measurement configurations is quite good, exhibiting appreciable divergence only in the lower portion of the shear layer at x/D=2.4. Since turbulent stress is a second-order statistic, a greater degree of measurement uncertainty can be expected compared to the mean velocities; therefore this level of consistency is certainly respectable. Conversely, the vertical turbulent stress shows discrepancies much like those seen in the mean vertical velocities of Fig. 10. Although the profile shapes are similar for the two-component and stereoscopic data, both a magnitude difference and a velocity offset can be observed in the profiles. These are attributable to the perspective error in the two-component measurements.

To be sure, a proper assessment of the comparison between the two PIV configurations cannot be performed until a thorough uncertainty analysis has been completed, which is not yet available at the time this is written. Nonetheless, the agreement in the data for the streamwise velocity component, both mean and turbulent stress, is quite striking, whereas the vertical component shows discrepancies consistent with the known effects of perspective error due to the camera angle. Therefore, although this two-component configuration is useful for visualizing the flow within the cavity and identifying turbulent eddies, quantitative values in the vertical direction are in error.

Vortex Identification

The determination of the large-scale turbulent eddies in the shear layer is not trivial. Vortices that are evident in the velocity field in one convection reference frame can be hidden in another [40]. This is key in the present flowfield, since the convection velocity varies greatly through the shear layer and into the recirculation region of the cavity. However, the swirling strength (known more briefly as swirl) often is used to identify vortices from vector fields because it has the advantages of insensitivity to convection frame and, unlike vorticity, is affected only by rotation and not shear [41].

The instantaneous vector field for the 5 × 5 cavity shown in Fig. 6c is repeated in Fig. 12a, but here the contour plot behind the vectors is the swirl (normalized to its maximum). This is a fixed reference frame of convection velocity $U_c=0.0U_\infty$, i.e., the laboratory reference frame. Several eddies are prominently discovered by the swirl field, but are less clear in the velocity field. For example, the peak in the swirl field seen at x/D=1.3 and y/D=-0.1 does appear to coincide with an elongated vortex, though not perfectly. Conversely, the two swirl peaks located firstly at x/D=2.7 and y/D=0.2 and secondly at x/D=3.2 and y/D=0.1 do not coincide with obvious vortices in the vector field. Another vortex at x/D=4.0 and y/D=-0.4 is apparent in the velocity vectors but only weakly in swirl.

If the reference convection frame is switched to $U_c=0.5U_\infty$ by simply subtracting $0.5U_\infty$ from the streamwise component, shown in Fig. 12b, newly apparent eddies in the vector field now appear to align with peaks in the swirl field. The elongated vortex at x/D=1.3 and y/D=-0.1 that was weakly visible and off-center in the $U_c=0.0U_\infty$ convection frame now aligns with multiple peaks in the swirl field. Similarly, the swirl peak at x/D=2.7 and y/D=0.2 that previously did not appear to coincide with a vortex now lies at the center of one. The vortex centered at x/D=1.3 and y/D=-0.1 actually is most evident in a convection frame of $U_c=0.4U_\infty$ and the vortex at x/D=2.7 and y/D=0.2 is clearest at $U_c=0.6U_\infty$, but the $U_c=0.5U_\infty$ reference frame is a reasonable compromise that clearly shows both vortices in a single plot.

The final reference frame shown is $U_c=1.0U_\infty$, given in Fig. 12c, which should reveal any passing turbulent eddies in the recirculation region. None are evident, which is consistent with the absence of any peaks in the swirl field. The same trend was found throughout the data set for the 5 × 5 cavity. Other investigations appear to have made a similar observation [14, 18, 20]. This suggests that large-scale turbulent eddies are prominent within the shear layer, but impingement upon the aft cavity wall tends to break them up into smaller turbulent scales.

Conclusions and Future Work

Particle image velocimetry measurements have been conducted for supersonic flow over a three-dimensional cavity of variable width. Data at Mach 1.5 are reported for cavities of length-to-width ratios of 5 × 5, 5 × 3, and 5 × 1, each with a length-to-depth ratio of slightly less than 5 × 1. Two different experimental configurations were used, one in which two cameras individually acquiring two-component data were combined to survey the entire streamwise extent of the cavity, and a second in which stereoscopic data of the cavity's aft end were obtained. The two-component configuration peered into the cavity at an angle, which introduced a bias error in the vertical

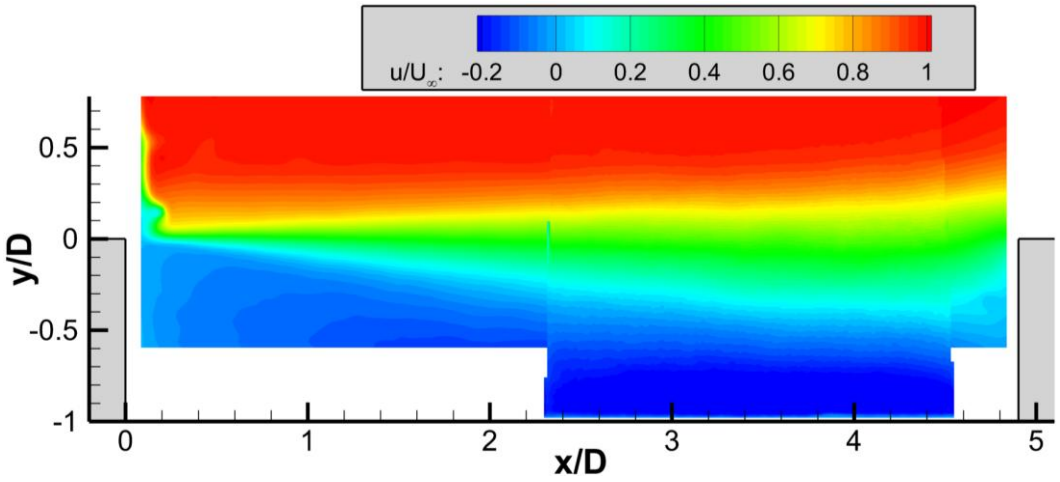

(a)

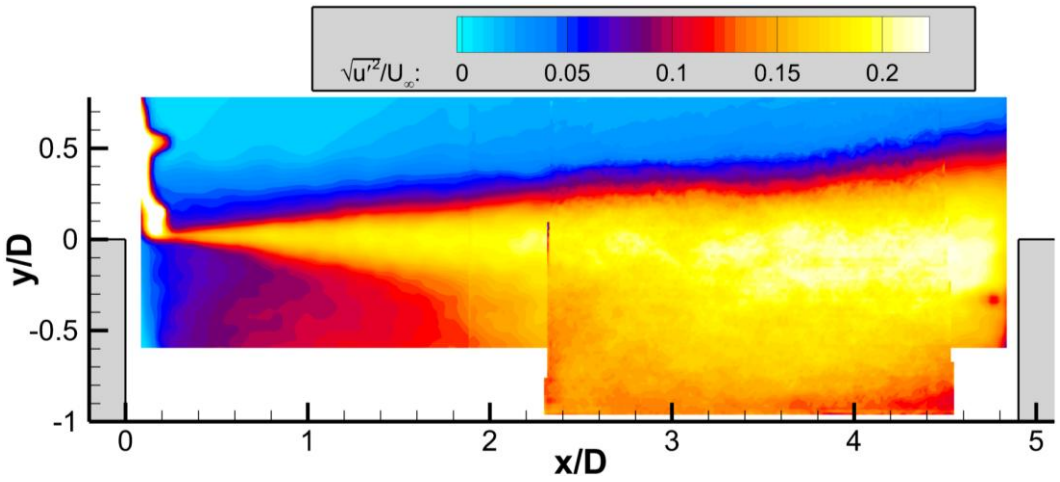

(b)

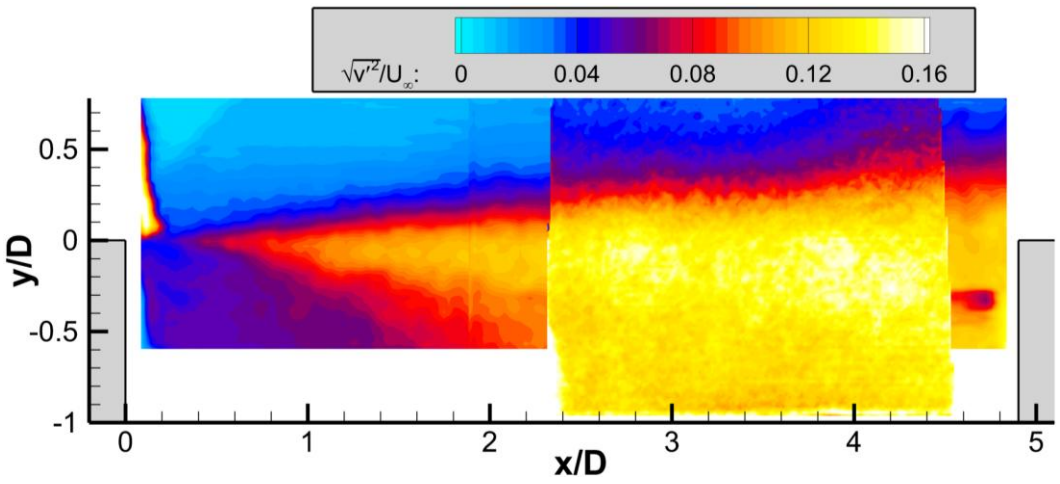

(c)

Fig. 9: Stereoscopic data overlaid on two-component data for the 127 × 127 mm^2 (5 × 5 inch^2) cavity. (a) mean streamwise velocity component; (b) streamwise turbulent stress; (c) vertical turbulent stress.

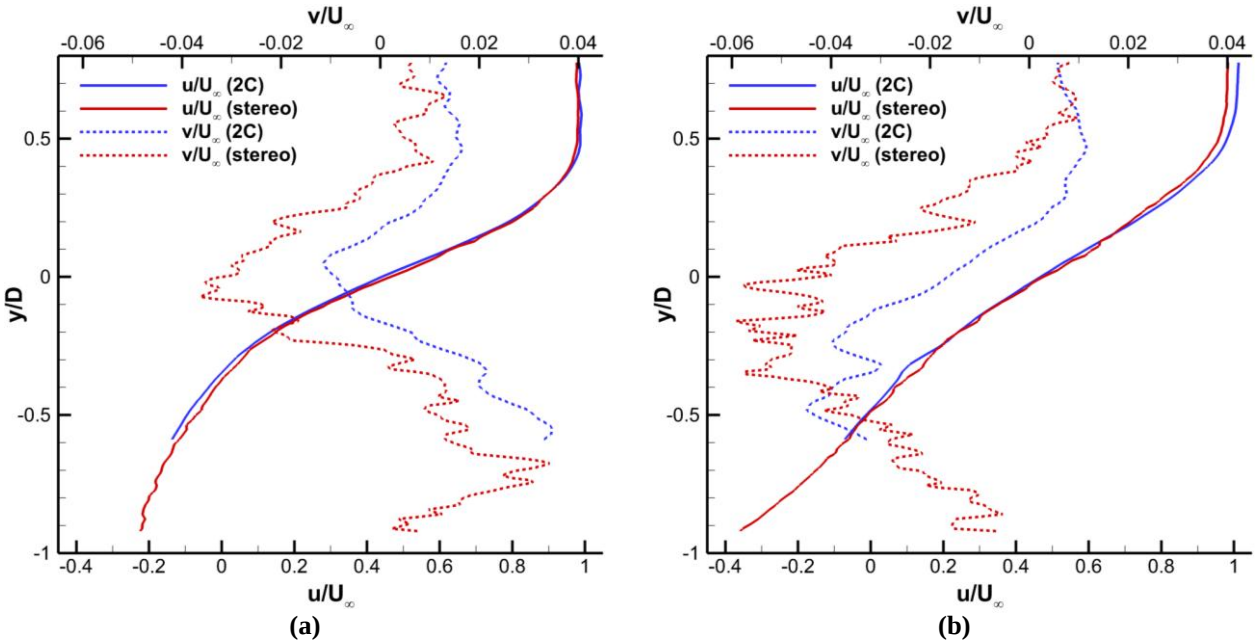

Fig. 10: Comparison of mean velocity data from the two-component and stereoscopic measurements; (a) ***x***/*D*=2.4; (b) ***x***/*D*=4.4.

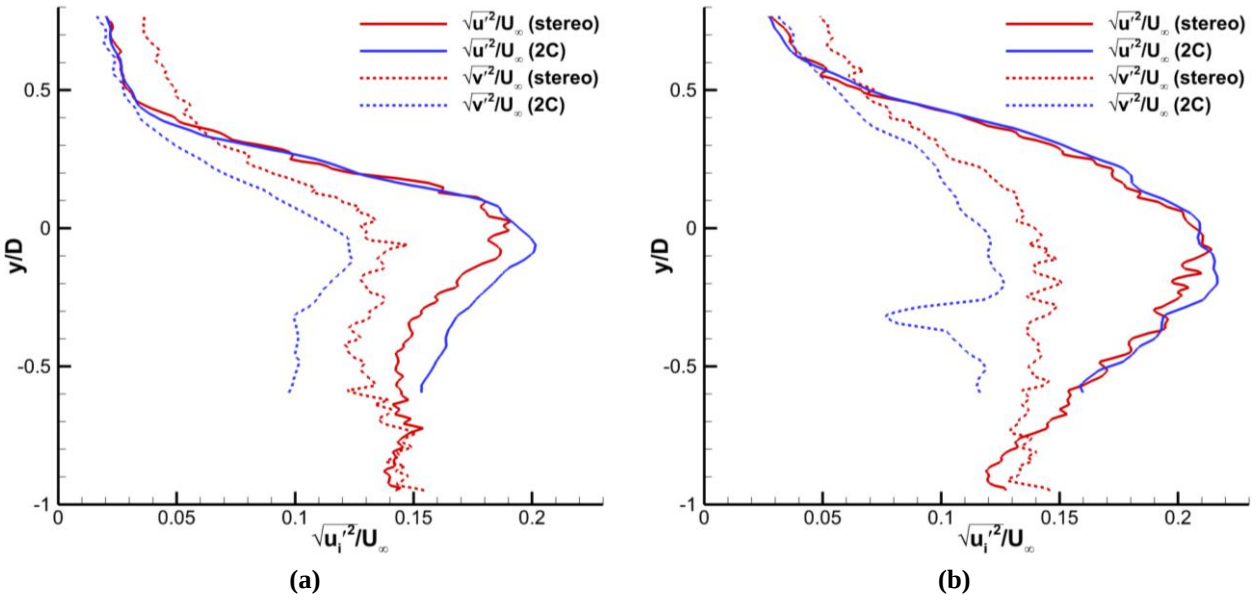

Fig. 11: Comparison of turbulent stress data from the two-component and stereoscopic measurements; (a) ***x***/*D*=2.4; (b) ***x***/*D*=4.4.

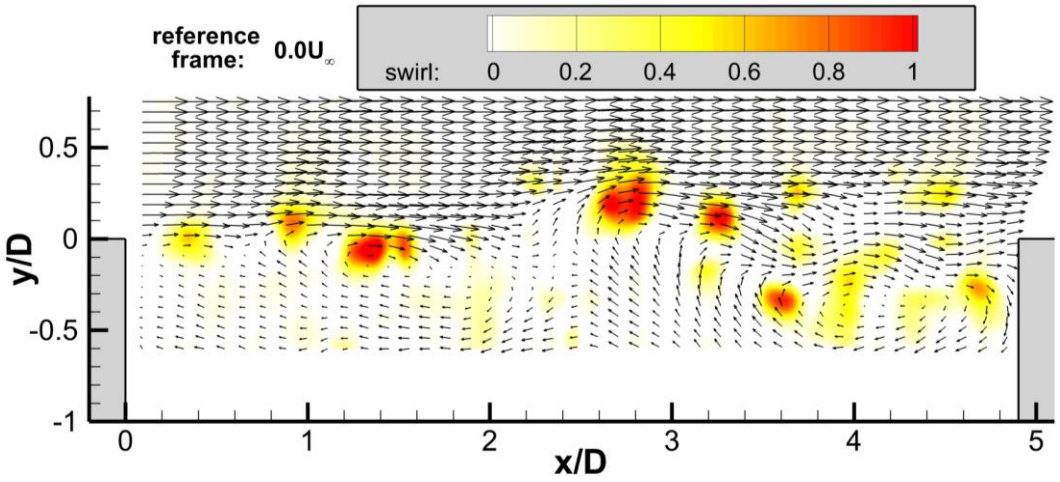

(a)

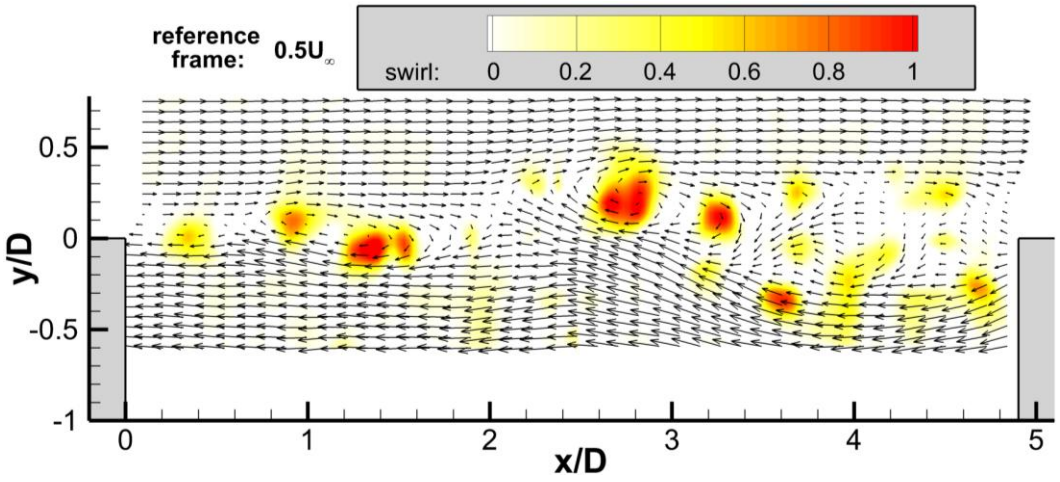

(b)

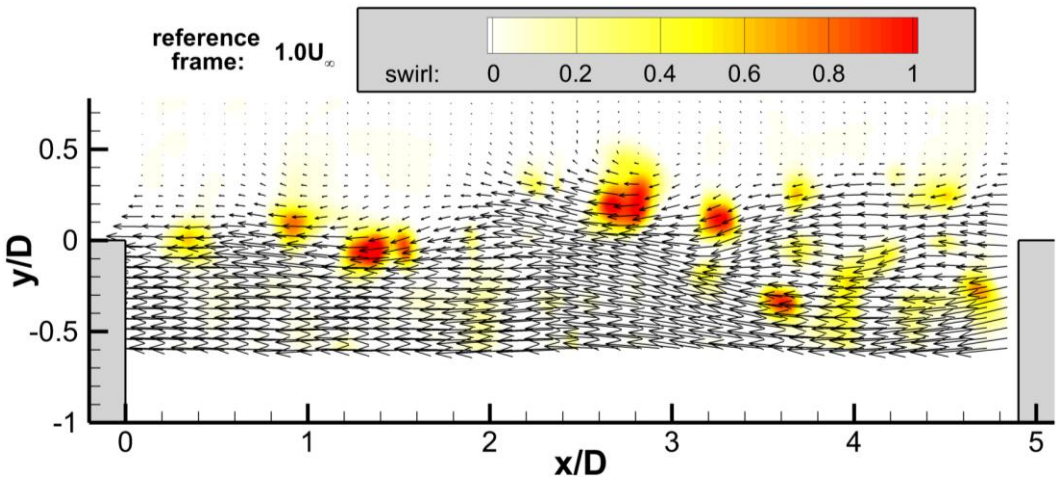

(c)

Fig. 12: Two-component velocity field data for a single realization of the 127 × 127 mm^2 (5 × 5 inch^2) cavity, overlaid on contours of swirling strength, and shown in three different convection reference frames. (a) U_c=0.0U_∞; (b) U_c=0.5U_∞; (c) U_c=1.0U_∞.

velocity component due to the perspective distortion, but this enabled data to reach 60% of the depth of the cavity for the widest geometry and only 10% for the narrowest. Conversely, the stereoscopic configuration employed a more complex camera angle into the cavity, in which the measurement of all three velocity components removes the presence of perspective error. The stereoscopic measurements reached to the cavity floor for the widest geometry and to about 30% depth for the narrowest. Data from the two configurations are in excellent agreement for the streamwise component, in both the mean velocity field and the turbulent intensity, but of course significant discrepancies in the vertical component occur due to the perspective error in the two-component measurements.

The data reveal the turbulent shear layer over the cavity and the recirculation region within it. Elevated levels of turbulence are found in the recirculation region, though still below the turbulent intensity of the shear layer. Instantaneous realizations of the large-scale eddies in the shear layer show that the eddy characteristics and shear layer undulations vary considerably in time, as does the strength of recirculation beneath it. The length-to-width ratio of the cavity was found to influence both the mean structure of the recirculation region and the turbulent nature of the shear layer. Of the three cavity widths studied, the middle width exhibited a shear layer with suppressed turbulent intensity compared to the widest and narrowest cavities. Additionally, the mean recirculation region for this middle-width cavity lay closer to the cavity floor and possessed weaker recirculation velocities.

Though the present document describes only data acquired at Mach 1.5, additional data are available at Mach 2.0 and 2.5. An initial examination of these higher Mach data is consistent with the observations at Mach 1.5, but a more detailed analysis is needed to seek any Mach effect in the results. The most interesting discovery is the change in the recirculation region and the shear layer turbulence intensity as a function of the length-to-width ratio of the cavity. Further investigation of this phenomenon is warranted, which could establish whether a spanwise acoustic tone is responsible. It also is possible that the characteristics of the turbulent eddies in the shear layer differ for the varied cavity widths, which can be investigated using the instantaneous realizations of the velocity field. Such studies are intended for future publications.

Finally, the present experiences implementing particle image velocimetry in a simple rectangular cavity have provided lessons that can be used to port the diagnostic to considerably more complex geometries replicating features found in real aircraft weapon bays. These measurement approaches allow the visualization of flow within the cavity without the need to install windows within such complex weapon bay geometries, making it of greater utility for tests of wind tunnel models of full flight vehicles and store separation.

Acknowledgments

The authors would like to thank John Henfling and Rusty Spillers, both of Sandia, for their support while operating the wind tunnel. Tom Grasser of Sandia designed the experimental hardware for the cavity configuration. Kurt Chankaya of Lockheed Martin Aeronautics provided considerable insight into weapon bay aerodynamics and guidance for the experimental planning.

References

[1] Krishnamurty, K., "Acoustic Radiation from Two-Dimensional Rectangular Cutouts in Aerodynamic Surfaces," NASA TN 3487, 1955.

[2] Zhang, X., and Rona, A., "An Observation of Pressure Waves around a Shallow Cavity," *Journal of Sound and Vibration*, Vol. 214, No. 4, 1998, pp. 771-778.

[3] Garg, S., and Cattafesta, L. N. III, "Quantitative Schlieren Measurements of Coherent Structures in a Cavity Shear Layer," *Experiments in Fluids*, Vol. 30, No. 1, 2001, pp. 123-134.

[4] Forestier, N., Jacquin, L., and Geffroy, P., "The Mixing Layer over a Deep Cavity at High-Subsonic Speed," *Journal of Fluid Mechanics*, Vol. 475, 2003, pp. 101-145.

[5] Kegerise, M. A., Spina, E. F., Garg, S., and Cattafesta, L. N. III, "Mode-Switching and Nonlinear Effects in Compressible Flow over a Cavity," *Physics of Fluids*, Vol. 16, No. 3, 2004, pp. 678-687.

[6] Rasmussen, C. C., Driscoll, J. F., Carter, C. D., and Hsu, K.-Y., "Characteristics of Cavity-Stabilized Flames in a Supersonic Flow," *Journal of Propulsion and Power*, Vol. 21, No. 4, 2005, pp. 765-768.

[7] Lazar, E., Elliott, G., and Glumac, N., "Control of the Shear Layer Above a Supersonic Cavity Using Energy Deposition," *AIAA Journal*, Vol. 46, No. 12, 2008, pp. 2987-2997.

[8] Grace, S. M., Dewar, W. G., and Wroblewski, D. E., "Experimental Investigation of the Flow Characteristics within a Shallow Wall Cavity for Both Laminar and Turbulent Upstream Boundary Layers," *Experiments in Fluids*, Vol. 36, No. 5, 2004, pp. 791-804.

[9] Murray, R. C., and Elliott, G. S., "Characteristics of the Compressible Shear Layer over a Cavity," *AIAA Journal*, Vol. 39, No. 5, 2001, pp. 846-856.

[10] Faure, T. M., Adrianos, P., Lusseyran, F., and Pastur, L., "Visualizations of the Flow Inside an Open Cavity at Medium Range Reynolds Numbers," *Experiments in Fluids*, Vol. 42, No. 2, 2007, pp. 169-184.

[11] Do, H., Cappelli, M. A., and Mungal, M. G., "Plasma Assisted Cavity Flame Ignition in Supersonic Flows," *Combustion and Flame*, Vol. 157, 2010, pp. 1783-1794.
[12] Hsu, K.-Y., Carter, C. D., Gruber, M. R., Barhorst, T., and Smith, S., "Experimental Study of Cavity-Strut Combustion in Supersonic Flow," *Journal of Propulsion and Power*, Vol. 26, No. 6, 2010, pp. 1237-1246.
[13] Lin, J.-C., and Rockwell, D., "Organized Oscillations of Initially Turbulent Flow Past a Cavity," *AIAA Journal*, Vol. 39, No. 6, 2001, pp. 1139-1151.
[14] Ashcroft, G., and Zhang, X., "Vortical Structures over Rectangular Cavities at Low Speed," *Physics of Fluids*, Vol. 17, No. 1, 2005, 015104.
[15] Ukeiley, L., and Murray, N., "Velocity and Surface Pressure Measurements in an Open Cavity," *Experiments in Fluids*, Vol. 38, No. 5, 2005, pp. 656-671.
[16] Hirahara, H., Kawahashi, M., Khan, M. U., and Hourigan, K., "Experimental Investigation of Fluid Dynamic Instability in a Transonic Cavity Flow," *Experimental Thermal and Fluid Science*, Vol. 31, No. 4, 2007, pp. 333-347.
[17] Little, J., Debiasi, M., Caraballo, E., and Samimy, M., "Effects of Open-Loop and Closed-Loop Control on Subsonic Cavity Flows," *Physics of Fluids*, Vol. 19, No. 6, 2007, 065104.
[18] Haigermoser, C., Vesely, L., Novara, M., and Onorato, M., "A Time-Resolved Particle Image Velocimetry Investigation of a Cavity Flow with a Thick Incoming Turbulent Boundary Layer," *Physics of Fluids*, Vol. 20, No. 10, 2008, 105101.
[19] Kang, W., Lee, S. B., and Sung, H. J., "Self-Sustained Oscillations of Turbulent Flows over an Open Cavity," *Experiments in Fluids*, Vol. 45, No. 4, 2008, pp. 693-702.
[20] Basley, J., Pastur, L. R., Lusseyran, F., Faure, T. M., and Delprat, N., "Experimental Investigation of Global Structures in an Incompressible Cavity Flow using Time-Resolved PIV," *Experiments in Fluids*, Vol. 50, No. 4, 2011, pp. 905-918.
[21] Bian, S., Driscoll, J. F., Elbing, B. R., and Ceccio, S. L., "Time Resolved Flow-Field Measurements of a Turbulent Mixing Layer over a Rectangular Cavity," *Experiments in Fluids*, Vol. 51, No. 1, 2011, pp. 51-63.
[22] Maull, D. J., and East, L. F., "Three-Dimensional Flow in Cavities," *Journal of Fluid Mechanics*, Vol. 16, 1963, pp. 620-632.
[23] Rockwell, D., and Knisely, C., "Observations of the Three-Dimensional Nature of Unstable Flow Past a Cavity," *Physics of Fluids*, Vol. 23, No. 3, 1980, pp. 425-431.
[24] Chung, K.-M., "Three-Dimensional Effect on Transonic Rectangular Cavity Flows," *Experiments in Fluids*, Vol. 30, No. 5, 2001, pp. 531-536.
[25] Larchevêque, L., Sagaut, P., and Labbé, O., "Large-Eddy Simulation of a Subsonic Cavity Flow Including Asymmetric Three-Dimensional Effects," *Journal of Fluid Mechanics*, Vol. 577, 2007, pp. 105-126.
[26] Brès, G. A., and Colonius, T., "Three-Dimensional Instabilities in Compressible Flow over Open Cavities," *Journal of Fluid Mechanics*, Vol. 599, 2008, pp. 309-339.
[27] Kannepalli, C., Chartrand, C., Birkbeck, R., Sinha, N., and Murray, N., "Computational Modeling of Geometrically Complex Weapons Bays," AIAA Paper 2011-2774, June 2011.
[28] Meganathan, A. J., "An Experimental Study of Open Cavity Flows at Low Subsonic Speeds," AIAA Paper 2002-0280, January 2002.
[29] Zhuang, N., Alvi, F. S., Alkislar, M. B., and Shih, C., "Supersonic Cavity Flows and their Control," *AIAA Journal*, Vol. 44, No. 9, 2006, pp. 2118-2128.
[30] Ritchie, S. A., Lawson, N. J., and Knowles, K., "Application of Particle Image Velocimetry to Transonic Cavity Flows," AIAA Paper 2005-1060, January 2005.
[31] Shen, P., "Supersonic Flow over a Deep Cavity for a Laser Application," *AIAA Journal*, Vol. 17, No. 2, 1979, pp. 216-219.
[32] Unalmis, O. H., Clemens, N. T., and Dolling, D. S., "Experimental Study of Shear-Layer/Acoustics Coupling in Mach 5 Cavity Flow," *AIAA Journal*, Vol. 39, No. 2, 2001, pp. 242-252.
[33] Poggie, J., and Smits, A. J., "Large-Scale Structures in a Compressible Mixing Layer over a Cavity," AIAA Journal, Vol. 41, No. 12, 2003, pp. 2410-2419.
[34] Samimy, M., and Lele, S. K., "Motion of Particles with Inertia in a Compressible Free Shear Layer," *Physics of Fluids A*, Vol. 3, No. 8, 1991, pp. 1915-1923.
[35] Melling, A., "Tracer Particles and Seeding for Particle Image Velocimetry," *Measurement Science and Technology*, Vol. 8, No. 12, 1997, pp. 1406-1416.
[36] Walker, S., "Two-Axes Scheimpflug Focusing for Particle Image Velocimetry," *Measurement Science and Technology*, Vol. 13, No. 1, 2002, pp. 1-12.
[37] Elsinga, G. E., Scarano, F., Wieneke, B., and van Oudheusden, B. W., "Tomographic Particle Image Velocimetry," *Experiments in Fluids*, Vol. 41, No. 6, 2006, pp. 933-947.
[38] Prasad, A. K., and Adrian, R. J., "Stereoscopic Particle Image Velocimetry Applied to Liquid Flows," *Experiments in Fluids*, Vol. 15, No. 1, 1993, pp. 49-60.
[39] Adrian, R. J., and Westerweel, J., *Particle Image Velocimetry*, Cambridge University Press, 2011, pp. 86-88.
[40] Adrian, R. J., Christensen, K. T., and Liu, Z.-C., "Analysis and Interpretation of Instantaneous Turbulent Velocity Fields," *Experiments in Fluids*, Vol. 29, No. 3, 2000, pp. 275-290.
[41] Zhou, J., Adrian, R. J., Balachandar, S., and Kendall, T. M., "Mechanisms for Generating Coherent Packets of Hairpin Vortices in Channel Flow," *Journal of Fluid Mechanics*, Vol. 387, 1999, pp. 353-396.